Inorganic Chemistry

pubs.acs.org/IC

Article

Vacancy-Ordered Hybrid Two-Dimensional Bi(III) Iodides with (100)-Oriented Dion-Jacobson Perovskite-Related Structures

Aditi Saraswat, Dheemahi Rao, Ankit Kumar Gupta, Bivas Saha, Gopalakrishnan Sai Gautam, and Pratap Vishnoi*

Cite This: *Inorg. Chem.* 2025, 64, 10279−10289

Read Online

ACCESS | Metrics & More | Article Recommendations | Supporting Information

ABSTRACT: Two-dimensional (2D) hybrid iodide perovskites, $(R{-}NH_3)_2MI_4$ and $(H_3N{-}R{-}NH_3)MI_4$ (R = alkyl group; M = divalent metal ion), are promising materials for optoelectronics. Traditionally, these compounds contain Pb^{2+} and Sn^{2+} ions in the M-site; however, concerns over the toxicity of Pb^{2+} and the instability of Sn^{2+} ions have driven interest in Bi^{3+} halide-based alternatives. This study reports two Dion-Jacobson type, vacancy-ordered 2D Bi−I perovskites: $(H_2DAC)Bi_{2/3}\square_{1/3}I_4$, with vacancy in every third metal site and $(H_2DAP)BiBi_{1/2}\square_{1/2}I_3{\cdot}(I_3)_{1/2}$, with vacancy in every second metal site (H_2DAC = *trans*-1,4-diammoniumcyclohexane, H_2DAP = 1,5-diammoniumpentane, and □ = vacancy). The band gaps of $(H_2DAC)Bi_{2/3}\square_{1/3}I_4$ and $(H_2DAP)Bi_{1/2}\square_{1/2}I_3{\cdot}(I_3)_{1/2}$ are 2.11 and 1.97 eV, respectively—both narrower than that of Pb^{2+}-based analogue $(H_2DAC)PbI_4$ (2.36 eV). These compounds show a positive photoresponse under light exposure, with the highest response observed in the case of $(H_2DAP)Bi_{1/2}\square_{1/2}I_3{\cdot}(I_3)_{1/2}$. This enhancement is attributed to the presence of I_3^- ions, which not only cross-link the perovskite layers and stabilize the H_2DAP cation in its *zigzag* conformation but also contribute to the frontier orbitals. DFT calculations corroborate these experimental results. Overall, this study introduces an approach for synthesizing hybrid Bi(III)-I perovskites, which may be further investigated as lead-free optoelectronic materials, including in perovskite photovoltaics.

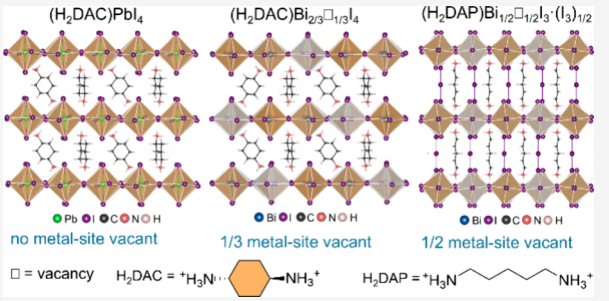

1. INTRODUCTION

Two-dimensional (2D) hybrid halide perovskites have gained a surge of interest in the semiconducting materials community, broadly due to their enhanced ambient stability and diverse chemical compositions compared to conventional AMX_3 perovskites (A = Cs^+, $CH_3NH_3^+$; M = Pb^{2+}, Sn^{2+}; X = Cl, Br, I).[1−3] The structure of a conventional AMX_3 perovskite consists of a corner-sharing framework of MX_6 octahedra connected via M−X−M linkages, with a monocation occupying the A-site.[4−6] The incorporation of bulky organic ammonium cation in the A-site disrupts the M−X−M connectivity along one of the three crystallographic directions, commonly the ⟨100⟩ direction. This leads to the formation of (100)-oriented Dion-Jacobson (DJ),[1,7] or Ruddlesden−Popper (RP) type 2D perovskites,[8] which typically adopt formulas $(H_3N{-}R{-}NH_3)MX_4$ or $(R{-}NH_3)_2MX_4$, respectively. Among these, DJ-type perovskites are generally more stable than their RP counterparts. An overwhelmingly large number of 2D halide perovskites containing Pb^{2+} and Sn^{2+} have been reported, but these metal ions have their own issues: Pb^{2+} is toxic, and Sn^{2+} is susceptible to oxidation.[1,8] Consequently, there has been a surge of interest in environmentally benign and stable alternatives. Bi^{3+} metal has emerged as a potential candidate due to its isoelectronic configuration $[Xe]4f^{14}5d^{10}6s^2$ to Pb^{2+} ion, as well as its comparable electronegativity and ionic size. This suggests that Bi^{3+} halide-based perovskites could potentially exhibit optical and electronic properties akin to those of Pb^{2+} halide-based analogs. However, trivalent Bi^{3+} ion cannot directly substitute divalent M^{2+} ion in $AM^{II}X_4$ perovskites. Instead, it can be combined with a monovalent metal ion (e.g., Ag^+) in equal proportion to form a layered double perovskite or with a metal vacancy to form a vacancy-ordered perovskite. Figure 1a,b shows schematic illustrations of the structures of a layered single-metal perovskite and a layered double perovskite, while Figure 1c,d illustrates the structures of their vacancy-ordered analogues. Although layered double perovskites offer a nontoxic and stable alternative,[9−15] their applications are generally limited by often nondispersive electronic structures and indirect band gaps.[16]

In the vacancy-ordered structures, metal vacancies compensate for the extra positive charge introduced by the replacement of a divalent cation with a trivalent cation. However, despite extensive studies on Dion−Jacobson-type

Received: March 19, 2025
Revised: April 23, 2025
Accepted: April 30, 2025
Published: May 12, 2025

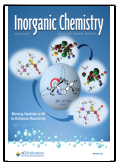

https://doi.org/10.1021/acs.inorgchem.5c01260
Inorg. Chem. 2025, 64, 10279−10289

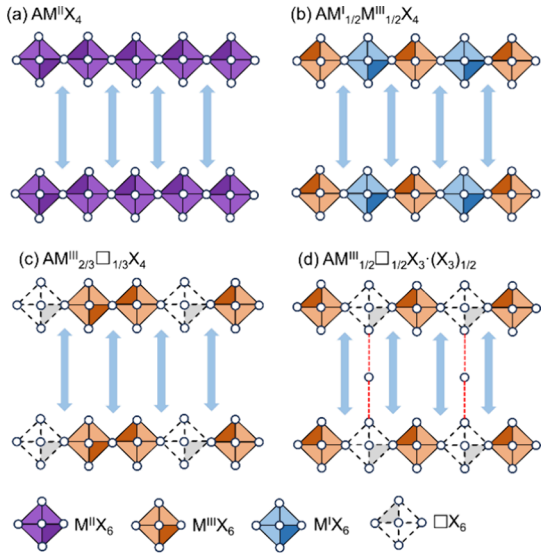

Figure 1. Schematic presentation (side view) of various compositional configurations possible for (100)-orientated Dion–Jacobson type n = 1 layered halide perovskites and their derived phases: (a) single-metal perovskite with all M-sites occupied by M^{2+} ions. (b) Double perovskites with all M-sites occupied by alternating M^{1+} and M^{3+} ions. (c) Vacancy-ordered perovskite with 2/3 of the M-sites occupied by M^{3+} ions and 1/3 are vacant. (d) Vacancy-ordered perovskite with 1/2 of the M-sites occupied by M^{3+} ions and 1/2 are vacant (A is a diamine; M^{I}, M^{II}, and M^{III} are mono-, di-, and trivalent metal ions, respectively; □ is a metal vacancy; X is a halide anion; X_3 is a trihalide ion). Note that vacant octahedra in the $AM^{III}_{1/2}\square_{1/2}X_3\cdot(X_3)_{1/2}$ structure are cross-linked by trihalide (shown by a dotted red line). The structure types shown in panels (a), (c), and (d) are the focus of this study.

layered $(H_3N{-}R{-}NH_3)MX_4$ perovskites comprising divalent metal ions and simple organic ammonium spacers, which have demonstrated a broad range of applications in the fields of spintronics and photodetectors,[17,18] 2D analogues that incorporate Bi^{3+} ions are rarely reported. Consequently, a deeper understanding of their synthesis, the templating effects of alkylamine cations, and their phase stability remains elusive. To the best of our knowledge, only four such systems have been reported. The first example, $(AE4T)Bi_{2/3}I_4$ (AE4T = 5,5′″-bis(aminoethyl)-2,2′:5′,2″:5″,2‴-quaterthiophene) was reported by Mitzi,[19] followed by three recent examples: $(4\text{-fluorophenethylammonium})_3BiI_6$,[20] $[(S)\text{-3-aminopyrrolidiniumI}]_2Bi_{2/3}I_4$,[21] and $(4\text{-bromophenethylammonium})_3BiI_6$.[22] Some of these metal-deficient compounds have been employed in low-dose X-ray detectors[20] and self-powered photodetectors,[22] highlighting their potentially useful properties. Prior studies have indicated that 2D Bi^{3+} halide perovskites with metal site vacancies are energetically unfavorable and can be synthesized with specific organic ammonium spacers that exhibit strong intermolecular interactions and a pronounced structure-directing effect on the perovskite layer.[12,19] These metal-deficient 2D perovskites share two structural features: (i) random distribution of metal-site vacancies over the available metal sites in the perovskite layers and (ii) strong interactions between the molecules of the organic ammonium spacer. The latter feature is considered critical for stabilizing the otherwise unfavorable metal-deficient 2D perovskite layer.[3,12,19] Conventional alkylamine cations are believed to lack such strong intermolecular interactions, often leading to the formation of nonperovskite hybrid halide structures (0D or 1D) with fully occupied metal sites.[23−27] However, it remains largely unexplored whether simple organic ammonium cations can be used as spacers in bismuth halide 2D structures, which is the focus of the current work.

In this work, we demonstrate the use of simple alkyldiammonium cations in the isolation of DJ perovskite-related vacancy-ordered hybrid 2D-type Bi(III) iodides: $(H_2DAC)Bi_{2/3}\square_{1/3}I_4$ and $(H_2DAP)Bi_{1/2}\square_{1/2}I_3\cdot(I_3)_{1/2}$ (H_2DAC = *trans*-1,4-diammoniumcyclohexane; H_2DAP = 1,5-diammoniumpentane; □ = vacancy). The former compound contains 2/3 occupied and 1/3 vacant metal sites, while the latter contains 1/2 occupied and 1/2 vacant metal sites. Their synthesis, X-ray structures, electronic structures, optical absorption, emission, and photoresponse properties have been investigated. Unlike conventional DJ-type 2D perovskites, these new structures offer the advantage of incorporating trivalent metal ions and excellent long-term phase stability in air. These structures show that while both rigid and flexible aliphatic diamine cations can act as spacers, a flexible spacer requires the support of triiodide ion (I_3^-) in the interlayer space. The I_3^- ion in $(H_2DAP)Bi_{1/2}\square_{1/2}I_3\cdot(I_3)_{1/2}$ not only compensates for the iodide ions (I^-) displaced due to reduced cationic charge in the perovskite layer but also boosts the optical absorption and electronic properties by reconstructing the electronic structure of the metal halide sublattice.[28,29] Additionally, we study a previously reported vacancy-free 2D perovskite, $(H_2DAC)PbI_4$,[30,31] as a reference to compare these two Bi(III) iodide systems.

2. RESULTS AND DISCUSSION

2.1. Synthesis and Characterization. Micrometer- to millimeter-size single crystals were hydrothermally synthesized in excess hydroiodic acid (see the Experimental Section for details). The reaction of Bi(III) acetate and *trans*-1,4-diaminocyclohexane at 160 °C, followed by slow cooling, yielded red crystals of $(H_2DAC)Bi_{2/3}\square_{1/3}I_4$. For the formation of this compound, a free I^- ion is required in the lattice to complete the six-coordination of the vacant octahedra. A stoichiometric amount of H_3PO_2 was added as a reducing agent in the reaction mixture to suppress the formation of polyiodide ions (e.g., I_3^-) and increase the concentration of I^- ions. Under similar reaction conditions, $(H_2DAP)Bi_{1/2}\square_{1/2}I_3\cdot(I_3)_{1/2}$ was synthesized from Bi(III) acetate and 1,5-diaminopentane in the absence of H_3PO_2. The formation of $(H_2DAP)Bi_{1/2}\square_{1/2}I_3\cdot(I_3)_{1/2}$ requires I_3^- ions rather than free I^- ions. In the absence of H_3PO_2, the availability of I_3^- ions enhances, favoring the formation of the I_3^- -containing phase. Conversely, the synthesis carried out in the presence of H_3PO_2 predominantly yielded $(H_2DAP)BiI_5$,[32] which exhibits a *zigzag* 1D structure devoid of I_3^- ion. In the 1D structure, the H_2DAP cation adopts a mixed *gauche* and *anti* conformation, while in $(H_2DAP)Bi_{1/2}\square_{1/2}I_3\cdot(I_3)_{1/2}$, the cation adopts a fully *anti* conformation (see the structural description below). These findings highlight that the I_3^- ion in $(H_2DAP)Bi_{1/2}\square_{1/2}I_3\cdot(I_3)_{1/2}$ not only stabilizes the H_2DAP cation in its fully *anti* conformation but also cross-links the perovskite layers with ordered metal site vacancies. Orange crystals of $(H_2DAC)PbI_4$ were obtained from the reaction of PbI_2 and *trans*-1,4-diaminocyclohexane at 160 °C, followed by slow cooling. In all of these reactions, the diamines became doubly protonated in the acidic medium, which is a crucial step for the isolation of these perovskites. The room temperature structures were determined from the single-crystal X-ray diffraction data. The

https://doi.org/10.1021/acs.inorgchem.5c01260
Inorg. Chem. 2025, 64, 10279−10289

structure refinement parameters are summarized in Table 1. The bond lengths and bond angles are listed in Tables S1−S3.

Table 1. Details of Single-Crystal X-ray Data Refinement

	$(H_2DAC)PbI_4$	$(H_2DAC)Bi_{2/3}\square_{1/3}I_4$	$(H_2DAP)Bi_{1/2}\square_{1/2}I_3 \cdot (I_3)_{1/2}$
empirical formula	$C_6H_{16}N_2PbI_4$	$C_3H_{12}NBi_{0.66}I_4$	$C_5H_{16}N_2Bi_{0.5}I_{4.5}$
formula weight	831.01	1144.69	1559.48
temperature	300(2) K	301(2) K	300(2) K
crystal system	monoclinic	monoclinic	orthorhombic
space group	$P2_1/c$	$P2_1/n$	$Cmcm$
unit cell dimensions			
a (Å)	10.6538(9)	13.202(2)	11.9026(3)
b (Å)	8.2069(9)	9.2415(12)	11.8606(3)
c (Å)	9.2298(10)	19.705(3)	23.9717(6)
α (°)	90	90	90
β (°)	91.841(4)	96.893(6)	90
γ (°)	90	90	90
volume	806.59(14)	2386.8(6)	3384.13(15)
Z	2	4	4
density (calculated)	3.422 mg/m^3	3.186 mg/m^3	3.061 mg/m^3
absorption coefficient	18.086 mm^{-1}	15.143 mm^{-1}	13.425 mm^{-1}
θ range for data collection	3.134 to 27.101°	2.44 to 29.22 °	2.424 to 27.105°
reflection collected	21407	85017	40876
data/restraints/parameters	1775/0/61	5247/0/176	2087/0/68
GoF on F^2	1.014	1.040	1.081
final R indices [I > 2sigma(I)]	R1 = 0.0293, wR2 = 0.0564	R1 = 0.0260, wR2 = 0.0582	R1 = 0.0408, wR2 = 0.0975
R indices (all data)	R1 = 0.0481, wR2 = 0.0625	R1 = 0.0333, wR2 = 0.0609	R1 = 0.0528, wR2 = 0.1035

The compounds were further characterized using powder X-ray diffraction (PXRD) and X-ray photoelectron spectroscopy (XPS) techniques. The compounds are stable under ambient conditions, with no decomposition observed during characterization or other measurements.

We shall describe the crystal structure of $(H_2DAC)PbI_4$ first, as the other two structures can be derived from it. Figure 2a,b shows the monoclinic $P2_1/c$ structure of $(H_2DAC)PbI_4$ with $[PbI_6]^{2-}$ octahedra forming (100)-oriented perovskite layers separated by H_2DAC dication along the crystallographic a-axis. Figure 2c shows that the adjacent octahedra within the perovskite layer are significantly tilted, with the Pb−I−Pb angle of 146.38 °, which is higher compared to most lead-iodide analogues containing diammonium spacers.[33,34] The octahedra also show a moderate local distortion, as indicated by the unequal Pb−I bond lengths and I−Pb−I bond angles (Table S1). The calculated bond distortion level (Δd) and bond angle variance (σ^2) are 5.64 × 10^{-5} and 18.43 deg^2, respectively. The eclipsed stacking of the perovskite layers confirms a DJ-type layer arrangement, with a noncovalent I···I distance of 4.303 Å between the axial iodides of the adjacent layers. This I···I distance is comparable with the sum of the van der Waals radii of two iodine (~4.4 Å).[1,35] The H_2DAC cation interlinks the perovskite layers via extensive N−H···I hydrogen bonds, as indicated by the nearest N···I distance of 3.594 Å (Table S1). The cation is tilted relative to the layer stacking direction (Figure S1a), optimizing both the I···I interaction between perovskite layers and the N−H···I interactions between the H_2DAC cation and the perovskite layer.

Figure 2d−f shows the structure of $(H_2DAC)Bi_{2/3}\square_{1/3}I_4$, which closely resembles that of $(H_2DAC)PbI_4$, with the key difference being the presence of ordered metal vacancies within the Bi(III)-iodide layer. The structure is composed of corner-sharing $[BiI_6]^{3-}$ octahedra, H_2DAC dication, and free monatomic iodide ions. While 1D *zigzag* chain structures of corner-sharing $[BiI_6]^{3-}$ octahedra with fully occupied metal sites have been reported in recent studies,[32,36] the distinctive

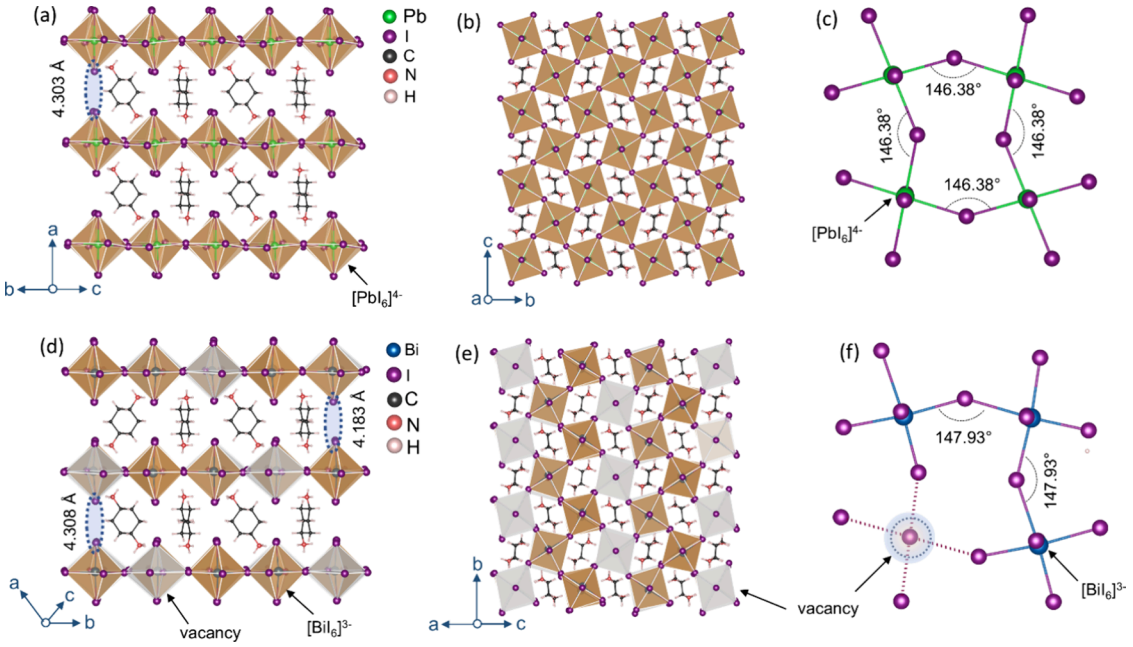

Figure 2. Side and top views of the crystal structures of (a, b) $(H_2DAC)PbI_4$ and (d, e) $(H_2DAC)Bi_{2/3}\square_{1/3}I_4$. Ball and stick models of the perovskite layers of (c) $(H_2DAC)PbI_4$ and (f) $(H_2DAC)Bi_{2/3}\square_{1/3}I_4$ are provided.

https://doi.org/10.1021/acs.inorgchem.5c01260
Inorg. Chem. 2025, 64, 10279−10289

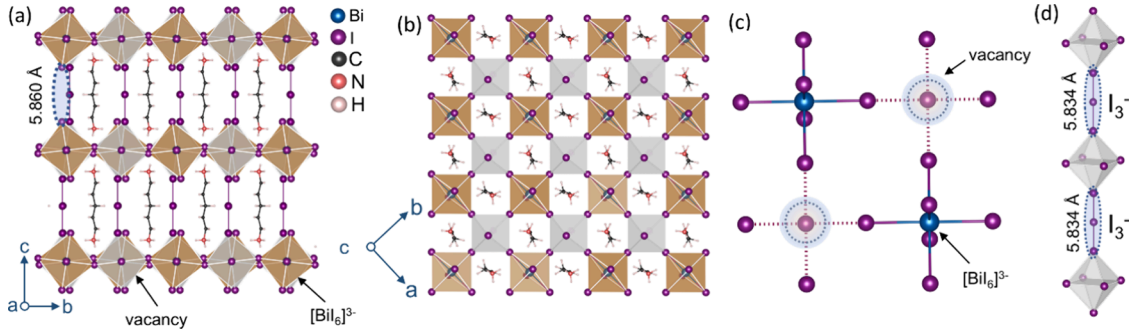

Figure 3. (a, b) Side and top views of the crystal structure of $(H_2DAP)Bi_{1/2}\square_{1/2}I_3{\cdot}(I_3)_{1/2}$. (c) Ball and stick models of the perovskite layer. (d) I_3^- ion, showing connection between the axial position of vacant metal sites.

structural feature of $(H_2DAC)Bi_{2/3}\square_{1/3}I_4$ is the formation of metal-site vacant octahedra between the 1D chains. The equatorial iodides of the $[BiI_6]^{3-}$ octahedra present on adjacent chains and the two monatomic iodides contribute to the vertices of the vacant polyhedra. This arrangement of Bi^{3+} and iodide ions is such that one out of every three metal sites is vacant, thereby forming a vacancy-ordered 2D layer of composition $[Bi_{2/3}\square_{1/3}I_4]^{2-}$. Compared to ideal octahedra in cubic symmetry, the $[BiI_6]^{3-}$ octahedra in $(H_2DAC)Bi_{2/3}\square_{1/3}I_4$ exhibit notable distortion as indicated by unequal Bi−I bond lengths and I−Bi−I bond angles (Table S2). This results in a high octahedral distortion level, with $\Delta d = 2.70 \times 10^{-3}$ and $\sigma^2 = 16.19$ deg^2. The shortest Bi−I bond involves the iodide shared between occupied and vacant octahedra, while the longest Bi−I bond involves the iodide shared between two occupied octahedra. This deflection of the Bi^{3+} ion from the center of the $[BiI_6]^{3-}$ octahedra is attributed to the stereochemically active $6s^2$ lone pair of electrons of the Bi^{3+} ion.[37] The Bi−I−Bi bridging angle (147.93 °) is similar to that of $(H_2DAC)PbI_4$ (Figure 2c,d). The H_2DAC dication separates the perovskite layer with noncovalent interlayer I···I distances of 4.308 and 4.183 Å. The interlayer gap in $(H_2DAC)Bi_{2/3}\square_{1/3}I_4$ is almost identical to $(H_2DAC)PbI_4$, with the H_2DAC dication adopting a similar tilted orientation along the stacking axis (i.e., *c*-axis) (Figure S1b).

Figure 3 shows the structure of $(H_2DAP)Bi_{1/2}\square_{1/2}I_3{\cdot}(I_3)_{1/2}$, which consists of isolated $[BiI_6]^{3-}$ octahedra, symmetric I_3^- ion and H_2DAP dication. The octahedra are only slightly distorted, as indicated by the bond lengths and bond angles (Table S3). The distortion parameters, $\Delta d = 4.67 \times 10^{-5}$ and $\sigma^2 = 1.32$ deg^2, are significantly lower than those of $(H_2DAC)PbI_4$ and $(H_2DAC)Bi_{2/3}\square_{1/3}I_4$. Within the *ab*-plane, the $[BiI_6]^{3-}$ octahedra are arranged such that every alternating metal site is vacant. As shown in Figure 3c,d, the equatorial positions of the vacant octahedra are occupied by the equatorial iodides of $[BiI_6]^{3-}$ octahedra, while the axial positions, pointing toward the interlayer gap, are occupied by the I_3^- ion. This arrangement results in the formation of a vacancy-ordered 2D monolayer of the composition $[Bi_{1/2}\square_{1/2}I_3{\cdot}(I_3)_{1/2}]^{2-}$. A unique structural feature of this compound is that the vacant metal sites are cross-linked by I_3^- ion, which aligns parallel to the H_2DAP cation within the interlayer gap, resulting in layer stacking without any lateral displacement.[38] The I_3^- ion is symmetric with the I−I bond distance of 2.917 Å, consistent with the reported values.[28] The H_2DAP forms N−H···I hydrogen bonds with the $[BiI_6]^{3-}$ octahedra (Table S3). The H_2DAP cation, with an N−N distance of 7.369 Å, is longer than the I_3^- ion (5.834 Å) and therefore penetrates more deeply into the cavity in inorganic perovskite layers formed by the axial iodides (Figure S2). The depth of penetration (0.754 Å) is twice that of the H_2DAC cation in $(H_2DAC)PbI_4$ (0.367 Å) and $(H_2DAC)Bi_{2/3}\square_{1/3}I_4$ (0.367 Å). To our knowledge, this is the first report of an I_3^- ion accompanying a diammonium cation spacer in a 2D halide perovskite-related structure. Furthermore, the presence of the I_3^- ion is likely essential to stabilize the H_2DAP cation in its fully *anti* conformation.

Furthermore, we carried out Hirshfeld surface analysis of $(H_2DAC)Bi_{2/3}\square_{1/3}I_4$ and $(H_2DAP)Bi_{1/2}\square_{1/2}I_3{\cdot}(I_3)_{1/2}$ to visualize intermolecular interactions of $[BiI_6]^{3-}$ moieties with their surrounding entities in the crystal lattices (Figures S3 and S4). The analysis reveals that the N−H···I hydrogen bonding constitutes a major contribution to the intermolecular interactions, accounting for 86.7% of the total intermolecular interactions in the case of $(H_2DAC)Bi_{2/3}\square_{1/3}I_4$ and 85.8% in the case of $(H_2DAP)Bi_{1/2}\square_{1/2}I_3{\cdot}(I_3)_{1/2}$. Noncovalent I···I interaction contributes 7.4% in the case of $(H_2DAC)Bi_{2/3}\square_{1/3}I_4$ and 14.2% in the case of $(H_2DAP)Bi_{1/2}\square_{1/2}I_3{\cdot}(I_3)_{1/2}$.

The purity of the bulk samples was examined by comparing the powder X-ray diffraction (PXRD) patterns with the simulated patterns generated from the single-crystal X-ray diffraction data. The experimental PXRD data agree with the simulated patterns (Figure S5). The elemental composition was further confirmed by XPS spectroscopy, where the survey spectra show peaks corresponding to all elements present in the samples (Figures S6−S8, Table S4). The metal-to-halide ratio almost matches the ratio obtained from the X-ray structures (Table S5). Figure 4 shows the core-level XPS spectra of the metal and halide elements. In the Pb (4f) spectrum, two peaks are observed at the binding energies of 137.6 and 142.5 eV, which correspond to the Pb^{2+} $4f_{7/2}$ and $4f_{5/2}$ states, respectively. The Bi (4f) spectra show two peaks at binding energies of 158.4 ($4f_{7/2}$) and 163.6 eV ($4f_{5/2}$) for $(H_2DAC)Bi_{2/3}\square_{1/3}I_4$, and at 158.1 ($4f_{7/2}$) and 163.3 eV ($4f_{5/2}$) for $(H_2DAP)Bi_{1/2}\square_{1/2}I_3{\cdot}(I_3)_{1/2}$. The ∼5.0 eV separation between the two peaks in each of these three 4f spectra is due to the spin−orbit coupling (SOC)-induced splitting. The I (3d) spectra of all three samples show peaks at 618.5 and 630.0 eV, corresponding to the $3d_{5/2}$ and $3d_{3/2}$ states, respectively, with the SOC splitting of ∼11.5 eV. Peaks for the C (1s) and N (1s) states were observed at the expected binding energies of 284.4 and 401.1 eV, respectively (Figures S9−S11). Furthermore, the C 1s spectra reveal two peaks, suggesting two distinct chemical environments around the C atoms, i.e.,

https://doi.org/10.1021/acs.inorgchem.5c01260
Inorg. Chem. 2025, 64, 10279−10289

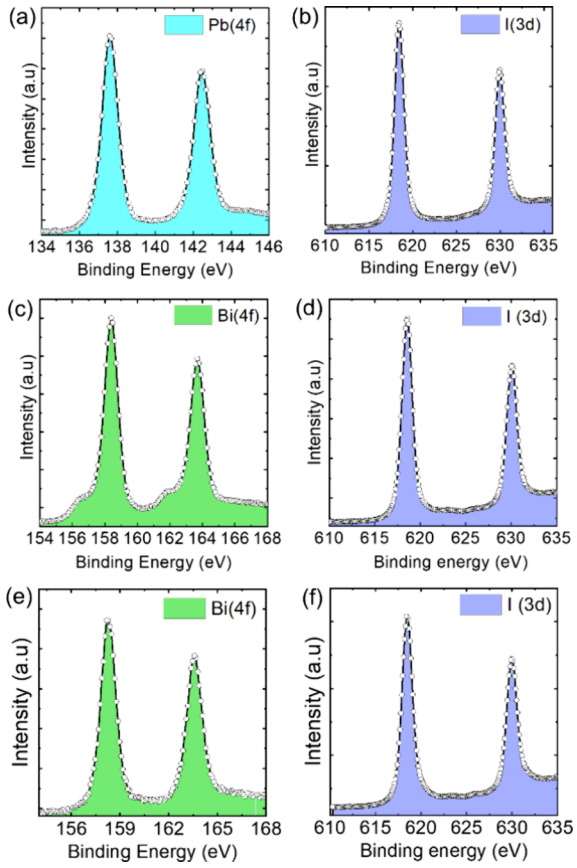

Figure 4. (a, b) Core level Pb (4f) and I (3d) XPS spectra of $(H_2DAC)PbI_4$. (c, d) Core level Bi (4f) and I (3d) XPS spectra of $(H_2DAC)Bi_{2/3}\square_{1/3}I_4$. (e, f) Core level Bi (4f) and I (3d) XPS spectra of $(H_2HDAP)Bi_{1/2}\square_{1/2}I_3{\cdot}(I_3)_{1/2}$.

the C atoms bonded to $-CH_2-$ and $-NH_3^+$ groups, with the latter appearing at higher binding energies.

2.2. Thermal Decomposition Analysis. We examined the thermal stability of all three compounds using thermogravimetric analysis (Figures S12–S14). For $(H_2DAC)PbI_4$, the initial decomposition occurs in the temperature range of 250–350 °C, with a mass loss of ∼45% corresponding to one $H_2DAC{\cdot}2I$ molecule per formula unit. The residue consists of PbI_2, then decomposes in the temperature range of 350–500 °C, as previously reported.[39] Similarly, $(H_2DAC)Bi_{2/3}\square_{1/3}I_4$ undergoes one-step decomposition, corresponding to the loss of one $H_2DAC{\cdot}2I$ molecule per formula unit, followed by evaporation of BiI_3 residue.[40] $(H_2DAP)Bi_{1/2}\square_{1/2}I_3{\cdot}(I_3)_{1/2}$ decomposes in two steps: the first weight loss of ∼17% in the temperature range of 150 − 200 °C is due to the loss of I_2 molecules, followed by the loss of one molecule of $H_2DAP{\cdot}2I$ per formula unit. The residue, corresponding to BiI_3, evaporates in the temperature range of 250–350 °C. Rapid decomposition of I_3^- containing hybrid perovskites has also been observed in other systems.[41] Notably, $(H_2DAC)PbI_4$ and $(H_2DAC)Bi_{2/3}\square_{1/3}I_4$, both containing rigid H_2DAC spacer, exhibit higher thermal stability than $(H_2DAP)Bi_{1/2}\square_{1/2}I_3{\cdot}(I_3)_{1/2}$, likely due to their corner-sharing structure.

2.3. Optical and Electronic Properties. We measured the diffuse reflectance spectra of all three samples after ball-milling and converted the data into pseudoabsorption spectra using the Kubelka–Munk function (Figure 5a). The optical band gaps were estimated by extrapolating the linear region of

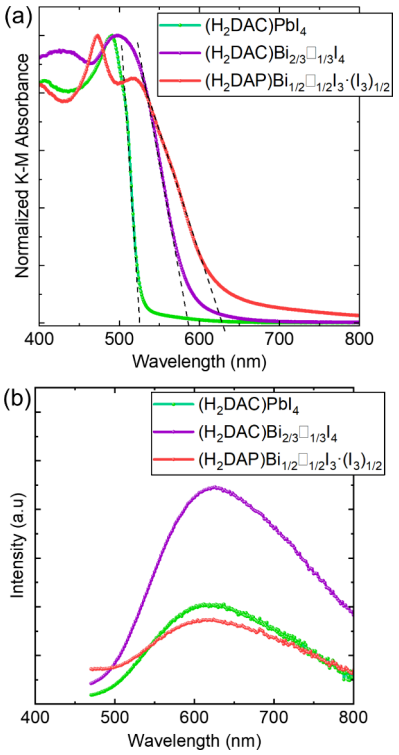

Figure 5. (a) UV–visible pseudoabsorption and (b) emission spectra.

the absorption edge to the wavelength axis. The band gap (E_g) of powdered $(H_2DAC)PbI_4$ is found to be 2.36 eV, which is consistent with previously reported values for $(H_2DAC)PbI_4$.[30] The band gap is slightly narrower than other DJ type $APbI_4$ (where A = diammonium cation) with highly tilted Pb–I–Pb angles, for example, (*m*-PDA)PbI_4 (E_g = 2.4 eV),[35] $(NH_3C_9H_{18}NH_3)PbI_4$ (E_g = 2.4 eV),[42] and [4-(aminomethyl)-piperidinium]PbI_4 (E_g = 2.4 eV).[1] The band gaps of $(H_2DAC)Bi_{2/3}\square_{1/3}I_4$ and $(H_2DAP)Bi_{1/2}\square_{1/2}I_3{\cdot}(I_3)_{1/2}$ are estimated to be 2.11 and 1.97 eV, respectively. The band gap of $(H_2DAC)Bi_{2/3}\square_{1/3}I_4$ closely matches that of previously reported Bi(III) deficient layered perovskite, such as (4-fluorophenethylammonium)$_3BiI_6$ (E_g = 2.1 eV),[20] and (4-bromophenethylammonium)$_3BiI_6$ (E_g = 2.0 eV).[22] The band gap of $(H_2DAP)Bi_{1/2}\square_{1/2}I_3{\cdot}(I_3)_{1/2}$ is narrower due to the presence of I_3^- ion, which is supported by the calculated band structures (discussed below). Notably, the band gaps of our Bi(III)-iodide systems are comparable with, or even narrower than, those of many 2D hybrid lead iodide perovskites.[17,43] This suggests that these Bi(III)-iodide compounds are efficient lead-free materials for visible-light harvesting and photo-detection applications. Figure 5b shows the emission spectra of $(H_2DAC)PbI_4$, $(H_2DAC)Bi_{2/3}\square_{1/3}I_4$, and $(H_2DAP)Bi_{1/2}\square_{1/2}I_3{\cdot}(I_3)_{1/2}$, with the emission bands centered at 620, 626, and 622 nm, respectively. The excited state lifetimes are 2.85 ns for $(H_2DAC)PbI_4$, 5.84 ns for $(H_2DAC)Bi_{2/3}\square_{1/3}I_4$, and 5.09 ns for $(H_2DAP)Bi_{1/2}\square_{1/2}I_3{\cdot}(I_3)_{1/2}$ (Figure S15, Table S6).

Additionally, we measured the XPS valence band spectra in the binding energy range of 0.0 to 20.0 eV (Figure 6a, Figures S16–S18) and estimated the position of valence band maxima (VBM) by extrapolating the linear portion of the lower energy band to the binding energy axis.[44] The spectrum of $(H_2DAC)PbI_4$ shows that the valence band edge lies at 0.75 eV, and is mainly dominated by I 5*p* states, which is consistent

https://doi.org/10.1021/acs.inorgchem.5c01260
Inorg. Chem. 2025, 64, 10279–10289

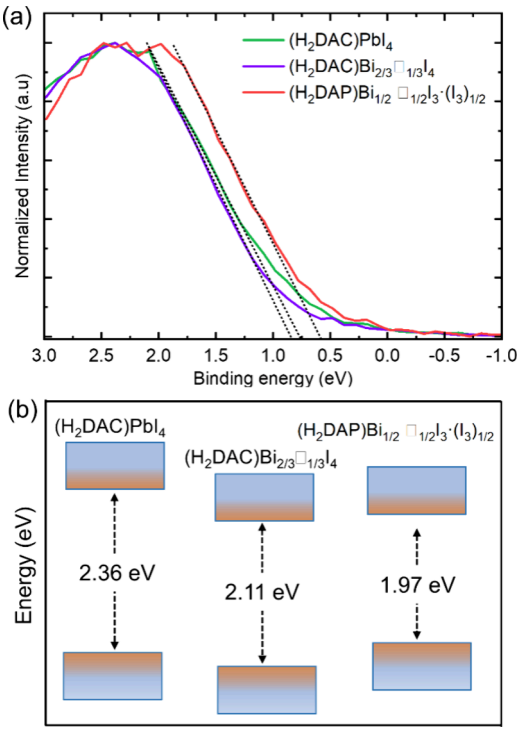

Figure 6. (a) XPS valence band spectra and (b) schematic presentation of band gap diagrams.

with the valence band spectra of commonly studied 3D (e.g., $MAPbI_3$)[45] and 2D perovskites.[46] Considering the optical band gap of 2.36 eV, the conduction band minimum (CBM) of $(H_2DAC)PbI_4$ was estimated to be 1.61 eV above the Fermi level. Similarly, the valence band spectra of $(H_2DAC)Bi_{2/3}\square_{1/3}I_4$ and $(H_2DAP)Bi_{1/2}\square_{1/2}I_3\cdot(I_3)_{1/2}$ show a major contribution from I 5*p* states near the band edge, with the band edge positions lying at the energy levels of 0.84 and 0.55 eV, respectively. The CBM was estimated to be 1.26 eV for $(H_2DAC)Bi_{2/3}\square_{1/3}I_4$ and 1.42 eV for $(H_2DAP)Bi_{1/2}\square_{1/2}I_3\cdot(I_3)_{1/2}$, both above the Fermi levels. Figure 6b shows the relative positions of VBM and CBM of all three compounds obtained by combining their optical band gaps and valence band spectra.

To better understand the underlying optical and electronic properties, we calculated the electronic band structures and the density of states (Figure 7) for all three compounds using density functional theory (DFT). The calculated structures have been given in Figures S19–S21. Our calculations indicate an indirect band gap of 2.24 eV for $(H_2DAC)PbI_4$ (Figure 7a), which is close to the optical band gap obtained from the UV–vis absorption spectrum. The band structure shows an almost parabolic CBM and relatively flatter VBM at the Γ point. $(H_2DAC)Bi_{2/3}\square_{1/3}I_4$ and $(H_2DAP)Bi_{1/2}\square_{1/2}I_3\cdot(I_3)_{1/2}$ also exhibit indirect band gaps (Figure 7b,c), with less dispersed CBM and VBM compared to $(H_2DAC)PbI_4$. The calculated band gap of $(H_2DAC)Bi_{2/3}\square_{1/3}I_4$ is 2.44 eV, while that of $(H_2DAP)Bi_{1/2}\square_{1/2}I_3\cdot(I_3)_{1/2}$ is 1.83 eV. The computed band gaps show a slight deviation from the experimental values, which is due to the limitations of the DFT method.

The calculated projected density of states (PDOS) of $(H_2DAC)PbI_4$, shown in Figure 7d, indicates that both iodide and lead orbitals contribute to the states at the VBM, with the majority of the contribution coming from the iodide orbitals. The lead orbitals are found to contribute more to the CBM than to the VBM. Similarly, the band extrema of $(H_2DAC)Bi_{2/3}\square_{1/3}I_4$ (Figure 7e) and $(H_2DAP)Bi_{1/2}\square_{1/2}I_3\cdot(I_3)_{1/2}$ (Figure 7f) are dominated by both iodide and bismuth orbitals. The iodide orbitals mainly contribute to the VBM, while the bismuth orbitals contribute to the CBM. In addition, the PDOS of $(H_2DAP)Bi_{1/2}\square_{1/2}I_3\cdot(I_3)_{1/2}$ shows that the I_3^- ion significantly reduces the band gap by reconstructing the band structure. Unlike $(H_2DAC)Bi_{2/3}\square_{1/3}I_4$, the presence of I_3^- ion in $(H_2DAP)Bi_{1/2}\square_{1/2}I_3\cdot(I_3)_{1/2}$ is not only affecting the band extrema but also leading to a larger dispersion of VBM as iodide orbitals contribute to both the bottom part of the conduction band and the upper part of the valence band. The band gap reduction due to the presence of I_3^- ion is consistent with the trend observed for the experimentally measured band gaps. The role of I_3^- ion in the electronic structure of $(H_2DAP)Bi_{1/2}\square_{1/2}I_3\cdot(I_3)_{1/2}$ is consistent with previously reported Bi(III)-iodide systems.[28] Furthermore, the calculated effective carrier masses of $(H_2DAP)Bi_{1/2}\square_{1/2}I_3\cdot(I_3)_{1/2}$ indicate charge transport in both in-plane (Γ → Y and Y → Γ) and out-of-plane directions (Γ → Z and Y → T). This is evident from the effective carrier masses of electrons and holes in both directions (Table S7). These results suggest that the presence of I_3^- ion enhances the light absorption capability of the material, making it a potential lead-free system for optoelectronic devices.

2.4. Photoconductivity. We investigated the photoresponse of $(H_2DAC)PbI_4$, $(H_2DAC)Bi_{2/3}\square_{1/3}I_4$, and $(H_2DAP)Bi_{1/2}\square_{1/2}I_3\cdot(I_3)_{1/2}$ under 30 s white light pulses using a Xe lamp. Silver paste was applied on the sample pellets to make contacts for electrical measurements, as schematically shown in Figure 8. The current–voltage (*I*-*V*) characteristic curves, measured from −10 to 10 V, indicate the formation of Ohmic contacts for all three compounds (Figure S22a–c). The transient current (*I*) curves for $(H_2DAC)PbI_4$, $(H_2DAC)Bi_{2/3}\square_{1/3}I_4$, and $(H_2DAP)Bi_{1/2}\square_{1/2}I_3\cdot(I_3)_{1/2}$ show that the current increases with time on shining light (Figure 9a–9c). This positive photoresponse is evident in *I*–*V* curves, where the slope under light exposure is steeper than in the dark (light off), suggesting an increase in conductance due to photogenerated carriers. In $(H_2DAC)PbI_4$, the current rises to about four times the dark current (I_{dark}) within a second and remains unchanged under continuous light exposure. When the light is turned off, the photocurrent returns to its original dark current value. This positive photocurrent on and off is repeatable in $(H_2DAC)PbI_4$, as shown in the representative five cycles (Figure 9a). Similarly, positive photoresponses have been observed for $(H_2DAC)Bi_{2/3}\square_{1/3}I_4$ and $(H_2DAP)Bi_{1/2}\square_{1/2}I_3\cdot(I_3)_{1/2}$ (Figure 9b,c), although the photocurrent recovery decreases over cycles of light on and off. The decrease in the magnitude of the photocurrent in successive cycles may result from carrier trapping in the photoactivated trap states or a reduction in available excited states due to the slow recombination of photogenerated carriers.[47] A similar photoresponse behavior has been observed in the case of $Cs_3Bi_2Br_9$, which has a vacancy-ordered perovskite structure with 1/3 of the octahedral sites vacant.[48] We fitted the transient photocurrent rise and decay to a single exponential function, yielding average rise and decay time constants of ∼0.17 and ∼0.50 s, respectively, for $(H_2DAC)PbI_4$ (Figure 9d, Table S8). These response times are relatively faster than those of analogous 2D Pb(II) iodides, such as $(C_6H_9C_2H_4NH_3)_2(CH_3NH_3)_{n-1}Pb_nI_{3n+1}$ (n = 1–4).[49] In

https://doi.org/10.1021/acs.inorgchem.5c01260
Inorg. Chem. 2025, 64, 10279–10289

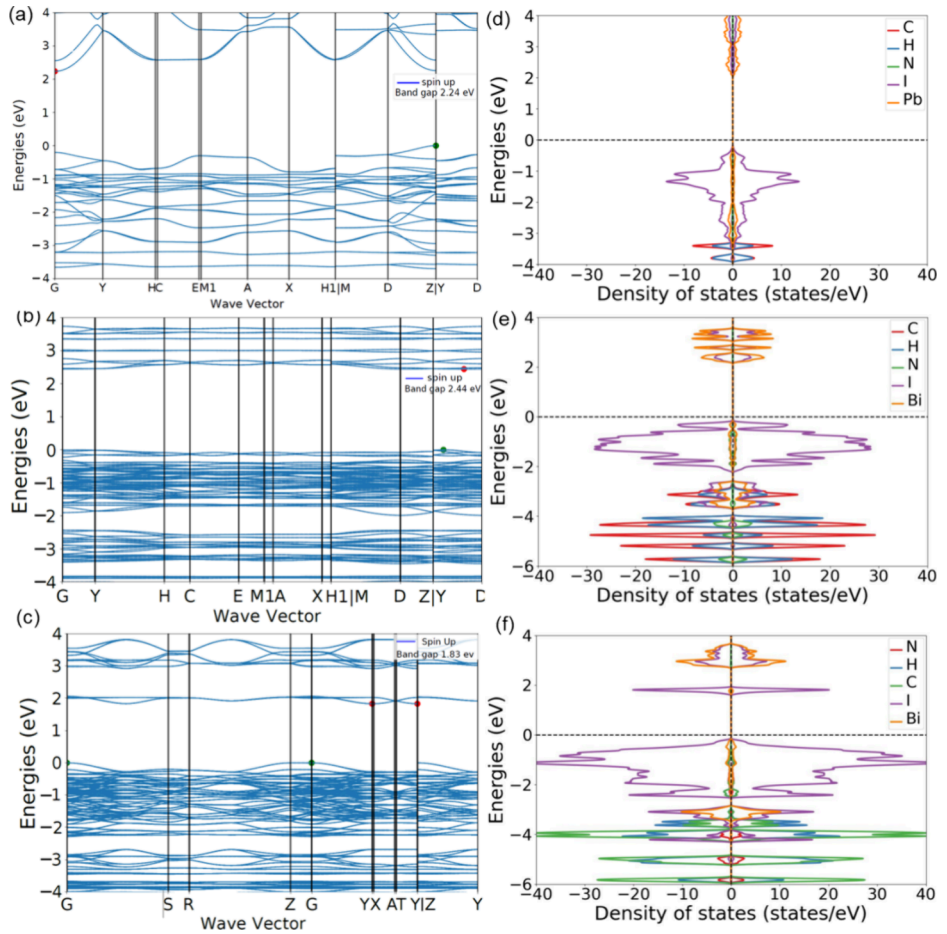

Figure 7. Electronic band structures of (a) $(H_2DAC)PbI_4$, (b) $(H_2DAC)Bi_{2/3}\square_{1/3}I_4$, and (c) $(H_2DAP)Bi_{1/2}\square_{1/2}I_3{\cdot}(I_3)_{1/2}$. The green and red dots indicate the VBM and the CBM, respectively. Projected DOS diagrams of (d) $(H_2DAC)PbI_4$, (e) $(H_2DAC)Bi_{2/3}\square_{1/3}I_4$, and (f) $(H_2DAP)Bi_{1/2}\square_{1/2}I_3{\cdot}(I_3)_{1/2}$.

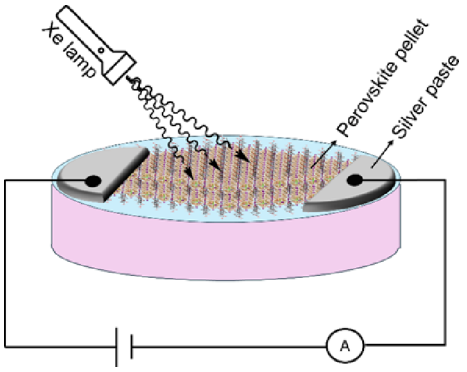

Figure 8. Schematic presentation of the photoresponse device.

contrast, the rates of photocurrent rise and decay in the case of our vacancy-ordered systems are slower. During the 30 s white light pulse, the current continuously rises by ~7 and ~70 nA for $(H_2DAC)Bi_{2/3}\square_{1/3}I_4$ and $(H_2DAP)Bi_{1/2}\square_{1/2}I_3{\cdot}(I_3)_{1/2}$, respectively. Upon turning the light off, the current gradually decays to its original dark current level in 30 s (Figure S22d,e, Tables S9 and S10). The average rise and decay times for $(H_2DAC)Bi_{2/3}\square_{1/3}I_4$ are 13.9 and 8.3 s (Figure S23), while for $(H_2DAP)Bi_{1/2}\square_{1/2}I_3{\cdot}(I_3)_{1/2}$, the average rise and decay times are 9.9 and 8.8 s, respectively (Figure 9e). Although $(H_2DAC)Bi_{2/3}\square_{1/3}I_4$ and $(H_2DAP)Bi_{1/2}\square_{1/2}I_3{\cdot}(I_3)_{1/2}$ contain metal vacancies, the latter compound shows higher photocurrent as well as a faster rise and decay of the photocurrent. This is attributed to the combination of more dispersed bands and enhanced charge transport in both out-of-plane and in-plane directions, facilitated by the triiodide ion present between the perovskite layers.[41]

We calculated the photo responsivity (R) by using the equation $R = (I_{light} - I_{dark})/(P \times A)$, where I_{light} = current on light illumination, I_{dark} = current after switching off the light, P = intensity of incident light, and A = device area.[50] The responsivity of $(H_2DAC)PbI_4$, $(H_2DAC)Bi_{2/3}\square_{1/3}I_4$, and $(H_2DAP)Bi_{1/2}\square_{1/2}I_3{\cdot}(I_3)_{1/2}$ for the first cycle are calculated to be 4.70×10^2, 3.6×10^2, and 59.2×10^2 nA/W, respectively. The slower photocurrent rise, lower responsivity, and longer lifetime decay for $(H_2DAC)Bi_{2/3}\square_{1/3}I_4$ indicate an increased number of trap states, most likely due to the vacancies in the material. $(H_2DAC)Bi_{2/3}\square_{1/3}I_4$ and $(H_2DAP)Bi_{1/2}\square_{1/2}I_3{\cdot}(I_3)_{1/2}$ also show a background (that is subtracted in Figure 9b,c) current during the photoresponse, possibly due to the migration of charges or alignment of the bonds under the influence of the electric field. Despite the presence of metal-site vacancies in these Bi(III)-based iodide systems, we observed positive photoresponses that are broadly similar in nature to some of the previously reported low-dimensional bismuth-based halide perovskites (Table S11).

https://doi.org/10.1021/acs.inorgchem.5c01260
Inorg. Chem. 2025, 64, 10279−10289

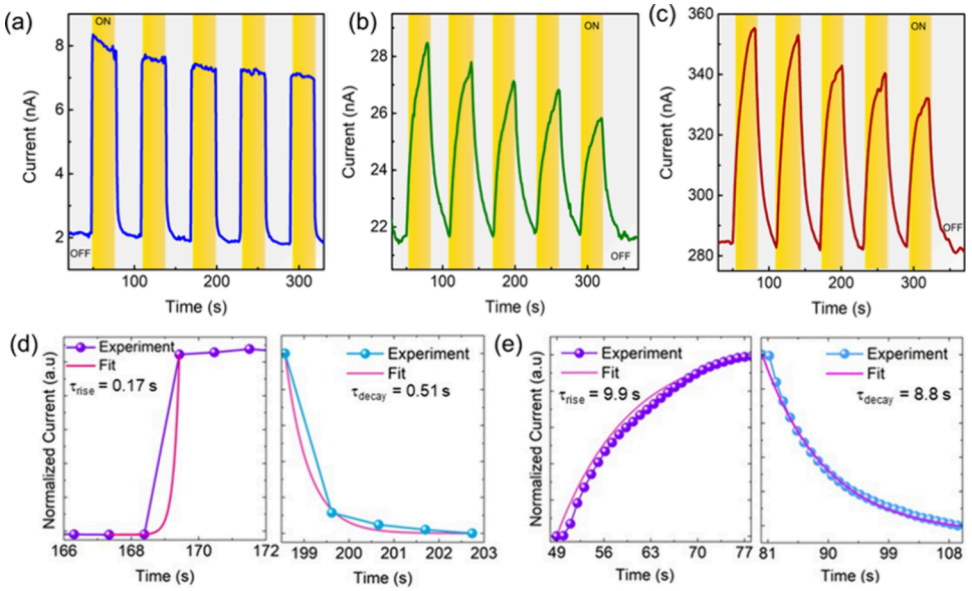

Figure 9. Photocurrent and time (I–t) response cycles for (a) $(H_2DAC)PbI_4$, (b) $(H_2DAC)Bi_{2/3}\square_{1/3}I_4$, and (c) $(H_2DAP)Bi_{1/2}\square_{1/2}I_3{\cdot}(I_3)_{1/2}$. The time duration of light illumination is marked with yellow regions. Single exponential fit of the photocurrent rise and decay of (d) $(H_2DAC)PbI_4$ and (e) $(H_2DAP)Bi_{1/2}\square_{1/2}I_3{\cdot}(I_3)_{1/2}$.

3. CONCLUSIONS

We have successfully synthesized and structurally characterized rare hybrid vacancy-ordered two-dimensional perovskite-related compounds $(H_2DAC)Bi_{2/3}\square_{1/3}I_4$ and $(H_2DAP)Bi_{1/2}\square_{1/2}I_3{\cdot}(I_3)_{1/2}$, where H_2DAC = *trans*-1,4-diammoniumcyclohexane, H_2DAP = 1,5-diammoniumpentane, and $\square$ = vacancy. These materials share structural similarity with conventional Dion–Jacobson-type layered perovskites in terms of the layer structure and the layer stacking pattern. Prior reports have suggested that hybrid Bi(III)-halides incorporating traditional alkylammonium cations often crystallize in nonperovskite 0D and 1D structures due to insufficient structural rigidity and weak intermolecular interactions.[3,12,19] However, our study showcases that by carefully selecting organic ammonium cations of appropriate size, shape, and charge and optimizing reaction conditions, the formation of nonperovskite phases can be suppressed in favor of 2D metal-deficient perovskite phases. The isolation of such compounds relies on a rigid interlayer spacer and free halide ions. While the rigidity of the spacer can be achieved by using a suitable organic amine precursor, the availability of free halide ions can be achieved by using a halide source (such as HI for iodide and triiodide) but, more importantly, through careful optimization of the synthesis conditions. Our finding also provides a novel approach to integrate organic diammonium cation and triiodide ion within the interlayer space. The triiodide ion plays a dual role of providing a rigid support to the flexible organic dication and contributing to the frontier orbitals, thereby enhancing the material's electronic properties. The versatility of these compounds has been further demonstrated by their photoresponses under white light. Particularly notable is the role of triiodide ion in $(H_2DAP)Bi_{1/2}\square_{1/2}I_3{\cdot}(I_3)_{1/2}$, introducing an additional electronic state below the conduction band minimum, and significantly reducing the band gap and enhancing the photoresponse. This work paves a new way for designing lead-free monometallic 2D halide perovskites and provides structural insights into their chemical tunability and optoelectronic properties. Unlike conventional Dion–Jacobson-type 2D perovskites, these new structures offer the advantage of incorporating trivalent metal ions, exhibiting excellent long-term phase stability in air. By using an appropriate organic ammonium spacer, this scaffold can be further expanded to incorporate various other trivalent metals, including magnetic metal ions, thereby paving new paths for exploring materials with properties beyond optoelectronics.

4. EXPERIMENTAL SECTION

4.1. Materials. Bismuth(III) acetate (Sigma-Aldrich; purity > 99.99%), PbI_2 (Sigma-Aldrich), *trans*-1,4-diaminocyclohexane (Tokyo Chemical Industry, purity = 98%), 1,5-diaminopentane (Sigma-Aldrich, purity > 97%), 50 wt % aqueous H_3PO_2 (Sigma-Aldrich), and stabilized 57 wt % aqueous HI (Sigma-Aldrich) were purchased from commercial vendors and used as such in the synthesis of the materials.

4.2. Synthesis of $(H_2DAC)PbI_4$. *Trans*-1,4-diaminocyclohexane (57.10 mg, 0.50 mmol), PbI_2 (115.20 mg, 0.25 mmol), and 57 wt % aqueous HI (3.0 mL) were taken in a 23 mL Teflon vial. The Teflon vial was then closed in a stainless-steel autoclave and heated in an oven at 160 °C for 24 h. After heating continuously at this temperature for 24 h, the autoclave was cooled to room temperature at 0.1 °C/min, which yielded needle-shaped orange crystals of $(H_2DAC)PbI_4$. The crystals were separated from the mother liquor, washed with copious amount of ethanol, and dried in a vacuum oven at 40 °C. Yield: 103 mg, 49.5% based on PbI_2 used in the reaction.

4.3. Synthesis of $(H_2DAC)Bi_{2/3}\square_{1/3}I_4$. *Trans*-1,4-diaminocyclohexane (57.10 mg, 0.50 mmol), $Bi(OAc)_3$ (96.50 mg, 0.25 mmol), 57 wt % aqueous HI (3.0 mL), and 50 wt % aqueous H_3PO_2 (100 μL, 0.75 mmol of H_3PO_2) were taken in a 23 mL Teflon vial. The Teflon vial was then closed in a stainless-steel autoclave and heated in an oven at 160 °C for 48 h. After continuous heating at this temperature for 48 h, the autoclave was cooled to room temperature at a cooling rate of 0.1 °C/min to obtain block-shaped red crystals of $(H_2DAC)Bi_{2/3}\square_{1/3}I_4$. The crystals were filtered, separated from the mother liquor, and dried on a Whatman filter paper. Yield: 199 mg, 69.5% based on $Bi(OAc)_3$ used in the reaction.

4.4. Synthesis of $(H_2DAP)Bi_{1/2}\square_{1/2}I_3{\cdot}(I_3)_{1/2}$. 1,5-Diaminopentane (51.0 mg, 0.50 mmol), $Bi(OAc)_3$ (96.5 mg, 0.25 mmol), and 57 wt % aqueous HI (4.0 mL) were taken in a 23 mL Teflon vial. The Teflon vial was then closed in a stainless-steel autoclave and heated in

https://doi.org/10.1021/acs.inorgchem.5c01260
Inorg. Chem. 2025, 64, 10279–10289

an oven at 160 °C for 48 h. Red crystals of $(H_2DAP)Bi_{1/2}\square_{1/2}I_3\cdot(I_3)_{1/2}$ were obtained on cooling the autoclave to room temperature at a cooling rate of 0.1 °C/min. The crystals were separated from the mother liquor and dried on a Whatman filter paper. Yield: 113 mg, 28% based on $Bi(OAc)_3$ used in the reaction.

4.5. Single Crystal X-ray Diffraction. X-ray diffraction data were collected for all three samples on a Bruker D8 Venture diffractometer, which is equipped with a Mo Kα X-ray source (wavelength = 0.71 Å), a graphite monochromator, and a photon detector. The X-ray source was operated with 50 kV power and 5 mA current. The X-ray quality crystals were screened under an optical microscope and mounted on quartz fiber using vacuum grease. *APEX3* software suite was used for the data collection, integration, and structure solutions. The structures were refined using the SHELXL program.[51] To ascertain that the Bi(III) ion has occupied the full site, the structure was first refined with the site having a fixed occupancy of 1.0, and then the occupancy was allowed to refine. The refinement was stable with a negligible change in the occupancy from 1.0 to 1.004, indicating that the Bi(III) ion occupies a full site in both $(H_2DAC)Bi_{2/3}\square_{1/3}I_4$ and (H_2DAP)-$Bi_{1/2}\square_{1/2}I_3\cdot(I_3)_{1/2}$ crystals. Furthermore, the refinement began to diverge if the site was forced to accept any other occupancy.

4.6. Photoresponse Measurements. Devices were made in pellet form by pressing powdered samples. The pellets are ∼2 mm thick and have ∼6 mm diameter. The copper wires were connected to the circular pellets by using silver paste. The distance between the contacts is 2−3 mm. The copper wires were connected to the circular pellets using silver paste. The Newport Xe-arc lamp (250−2400 nm) was used to illuminate the sample, and the current is measured using Keithley 2461 source meter at constant bias of 10 V. The photo response cycles were measured with 30 s light pulses of about 100 mW/cm^2 intensity with active areas of 2 × 6.5 mm^2, 2 × 6 mm^2, and 3 × 6.5 mm^2 for $(H_2DAC)PbI_4$, $(H_2DAC)Bi_{2/3}\square_{1/3}I_4$, and (H_2DAP)-$Bi_{1/2}\square_{1/2}I_3\cdot(I_3)_{1/2}$, respectively.

The photoresponse time rise and decay for the three compounds were calculated using single exponential growth and decay functions using the equations given below.[52]

$$\text{time growth: } I(t) = I_o + B_1\exp(t/\tau_1)$$

$$\text{time decay: } I(t) = I_o + B_1\exp(-t/\tau_1)$$

where I_0 = offset current, B_1 = amplitude of current, t = time, and τ = time constant for lifetime of carriers.

4.7. Electronic Structure Calculations. For calculating the band structures and density of states (DOS), we carried out density functional theory (DFT) simulations using the Vienna ab initio simulation package (VASP).[53,54] We employed the projector augmented-wave (PAW)[55] potentials in our calculations, and specifically used the H ($1s^1$), C ($2s^2$,$2p^2$), N ($2s^2$,$2p^3$), I ($5s^2$,$5p^3$), Pb ($6s^2$,$6p^2$), and Bi ($6s^2$,$6p^3$) potentials. We expanded the plane-wave basis up to a kinetic energy cutoff of 520 eV for all calculations. We sampled the irreducible Brillouin zone using Γ-centered Monkhorst−Pack[56] meshes with a density of at least 48 k-points per Å and used a Gaussian smearing of width 0.05 eV to integrate the Fermi surface. Bulk relaxation of all structures was done in two steps following previous literature:[57] (i) we relaxed the H atoms alone in our starting structures using selective dynamics to freeze the non-H atoms, followed by (ii) a full relaxation of all atom positions, cell shape, and cell volume without preserving symmetry. We relaxed all structures until the atomic forces reduced below |0.01| eV/Å, and total energies below 10^{-5} eV. We initialized the atomic magnetic moments with a nonzero value of 0.6 μB in a ferromagnetic configuration to facilitate structural relaxation. To optimize the bulk structures, we treated the electronic exchange-correlation interactions with the strongly constrained and appropriately normed (SCAN) functional.[58] For the DOS calculations, we used the converged ground state structure of each compound and applied the "fake" self-consistent field (SCF) procedure, with a mesh density of at least 96 k-points per Å. Note that the set of k-points sampled during the structure relaxation was preserved with their original weights, while the newly introduced k-points were sampled with zero weights within the fake-SCF procedure. Similarly, for band structure calculations, we used the Setyawan−Curtarolo scheme, as implemented in the pymatgen package, for identifying high symmetry k-paths to be sampled.[59,60] We did not include spin−orbit coupling (SOC) in our calculations to minimize computational costs, given that two of the structures have an excess of 150 atoms in their unit cells. Given the good agreement we have on the calculated band structures and band gaps with experimental results, we postulate that spin−orbit coupling may not have a significant effect on the systems reported in this study.

■ ASSOCIATED CONTENT

Supporting Information

The Supporting Information is available free of charge at https://pubs.acs.org/doi/10.1021/acs.inorgchem.5c01260.

Additional experimental details, crystallographic tables, bond lengths and bond angles tables, additional X-ray structures, optimized structures, Hirshfeld surfaces diagrams, powder XRD patterns, XPS spectra, valence band XPS spectra, time-resolved photoluminescence spectra, additional photoresponse plots, and thermogravimetric analysis (TGA) plots for all compounds (PDF)

Accession Codes

Deposition Numbers 2357610−2357612 contain the supplementary crystallographic data for this paper. These data can be obtained free of charge via the joint Cambridge Crystallographic Data Centre (CCDC) and Fachinformationszentrum Karlsruhe Access Structures service.

■ AUTHOR INFORMATION

Corresponding Author

Pratap Vishnoi − *New chemistry Unit and International Centre for Materials Science, Jawaharlal Nehru Centre for Advanced Scientific Research, Bengaluru 560064, India; School of Advacned Materials, Jaweaharlal Nehru Centre for Advanced Scientific Research, Bengaluru 560064, India;* orcid.org/0000-0003-4717-9346; Email: pvishnoi@jncasr.ac.in

Authors

Aditi Saraswat − *New chemistry Unit and International Centre for Materials Science, Jawaharlal Nehru Centre for Advanced Scientific Research, Bengaluru 560064, India*

Dheemahi Rao − *International Centre for Materials Science and Chemistry and Physics of Materials Unit, Jawaharlal Nehru Centre for Advanced Scientific Research, Bengaluru 560064, India;* orcid.org/0000-0002-1952-3210

Ankit Kumar Gupta − *Department of Materials Engineering, Indian Institute of Science, Bengaluru 560012, India*

Bivas Saha − *International Centre for Materials Science and Chemistry and Physics of Materials Unit, Jawaharlal Nehru Centre for Advanced Scientific Research, Bengaluru 560064, India*

Gopalakrishnan Sai Gautam − *Department of Materials Engineering, Indian Institute of Science, Bengaluru 560012, India;* orcid.org/0000-0002-1303-0976

Complete contact information is available at: https://pubs.acs.org/10.1021/acs.inorgchem.5c01260

Notes

The authors declare no competing financial interest.

https://doi.org/10.1021/acs.inorgchem.5c01260
Inorg. Chem. 2025, 64, 10279−10289

■ ACKNOWLEDGMENTS

This work was financially supported by the Science & Engineering Research Board (SERB) of the Govt of India through a Core Research Grant (grant no. CRG/2022/009230) to P.V. The authors thank Prof. C. N. R. Rao (FRS) for his kind support.

■ DEDICATION

Dedicated to Prof. Ramaswamy Murugavel on his 60th birthday.

■ REFERENCES

(1) Mao, L.; Ke, W.; Pedesseau, L.; Wu, Y.; Katan, C.; Even, J.; Wasielewski, M. R.; Stoumpos, C. C.; Kanatzidis, M. G. Hybrid Dion-Jacobson 2D Lead Iodide Perovskites. *J. Am. Chem. Soc.* **2018**, *140* (10), 3775−3783.

(2) Lee, M. M.; Teuscher, J.; Miyasaka, T.; Murakami, T. N.; Snaith, H. J. Efficient Hybrid Solar Cells Based on Meso-Superstructured Organometal Halide Perovskites. *Science.* **2012**, *338* (6107), 643−647.

(3) Saparov, B.; Mitzi, D. B. Organic−Inorganic Perovskites: Structural Versatility for Functional Materials Design. *Chem. Rev.* **2016**, *116* (7), 4558−4596.

(4) Vishnoi, P.; Rao, C. N. R. Temperature and Pressure Induced Structural Transitions of Lead Iodide Perovskites. *J. Mater. Chem. A* **2023**, *12* (1), 19−37.

(5) Kojima, A.; Teshima, K.; Shirai, Y.; Miyasaka, T. Organometal Halide Perovskites as Visible-Light Sensitizers for Photovoltaic Cells. *J. Am. Chem. Soc.* **2009**, *131* (17), 6050−6051.

(6) Burschka, J.; Pellet, N.; Moon, S.-J.; Humphry-Baker, R.; Gao, P.; Nazeeruddin, M. K.; Grätzel, M. Sequential Deposition as a Route to High-Performance Perovskite-Sensitized Solar Cells. *Nature* **2013**, *499* (7458), 316−319.

(7) Vishwajith, N. S.; Sharma, M. K.; Jain, I.; Vishnoi, P. $[NH_3(CH_2)_4NH_3]SnX_4$ (X = Br, I): Dion−Jacobson Type 2-D Perovskites with Short Interlayer Spacing. *Dalt. Trans.* **2024**, *53* (6), 2465−2470.

(8) Gong, J.; Hao, M.; Zhang, Y.; Liu, M.; Zhou, Y. Layered 2D Halide Perovskites beyond the Ruddlesden−Popper Phase: Tailored Interlayer Chemistries for High-Performance Solar Cells. *Angew. Chem., Int. Ed.* **2022**, *61* (10), No. e202112022.

(9) Bi, L. Y.; Hu, Y. Q.; Li, M. Q.; Hu, T. L.; Zhang, H. L.; Yin, X. T.; Que, W. X.; Lassoued, M. S.; Zheng, Y. Z. Two-Dimensional Lead-Free Iodide-Based Hybrid Double Perovskites: Crystal Growth, Thin-Film Preparation and Photocurrent Responses. *J. Mater. Chem. A* **2019**, *7* (34), 19662−19667.

(10) Lassoued, M. S.; Bi, L.-Y.; Wu, Z.; Zhou, G.; Zheng, Y.-Z. Piperidine-Induced Switching of the Direct Band Gaps of Ag(I)/Bi(III) Bimetallic Iodide Double Perovskites. *J. Mater. Chem. C* **2020**, *8* (16), 5349−5354.

(11) Yao, Y.; Kou, B.; Peng, Y.; Wu, Z.; Li, L.; Wang, S.; Zhang, X.; Liu, X.; Luo, J. $(C_3H_9NI)_4AgBiI_8$: A Direct-Bandgap Layered Double Perovskite Based on a Short-Chain Spacer Cation for Light Absorption. *Chem. Commun.* **2020**, *56* (21), 3206−3209.

(12) Jana, M. K.; Janke, S. M.; Dirkes, D. J.; Dovletgeldi, S.; Liu, C.; Qin, X.; Gundogdu, K.; You, W.; Blum, V.; Mitzi, D. B. Direct-Bandgap 2D Silver-Bismuth Iodide Double Perovskite: The Structure-Directing Influence of an Oligothiophene Spacer Cation. *J. Am. Chem. Soc.* **2019**, *141* (19), 7955−7964.

(13) Binwal, D. C.; Mudoi, P. P.; Panda, D. P.; Vishnoi, P. Molybdenum Chloride Double Perovskites: Dimensionality Control of Optical and Magnetic Properties. *Chem. Sci.* **2023**, *14* (15), 3982−3989.

(14) Connor, B. A.; Leppert, L.; Smith, M. D.; Neaton, J. B.; Karunadasa, H. I. Layered Halide Double Perovskites: Dimensional Reduction of $Cs_2AgBiBr_6$. *J. Am. Chem. Soc.* **2018**, *140* (15), 5235−5240.

(15) Li, Q. W.; Bi, L. Y.; Lassoued, M. S.; Luo, Q. C.; Yan, R.; Ding, X. K.; Gou, G. Y.; Zheng, Y. Z. Two-Dimensional Semiconducting Cu(I)/Sb(III) Bimetallic Hybrid Iodides with a Double Perovskite Structure and Photocurrent Response. *Nanoscale* **2023**, *15* (11), 5265−5273.

(16) Connor, B. A.; Su, A. C.; Slavney, A. H.; Leppert, L.; Karunadasa, H. I. Understanding the Evolution of Double Perovskite Band Structure upon Dimensional Reduction. *Chem. Sci.* **2023**, *14* (42), 11858−11871.

(17) Park, I.-H.; Kwon, K. C.; Zhu, Z.; Wu, X.; Li, R.; Xu, Q.-H.; Loh, K. P. Self-Powered Photodetector Using Two-Dimensional Ferroelectric Dion−Jacobson Hybrid Perovskites. *J. Am. Chem. Soc.* **2020**, *142* (43), 18592−18598.

(18) Park, I.-H.; Zhang, Q.; Kwon, K. C.; Zhu, Z.; Yu, W.; Leng, K.; Giovanni, D.; Choi, H. S.; Abdelwahab, I.; Xu, Q.-H.; Sum, T. C.; Loh, K. P. Ferroelectricity and Rashba Effect in a Two-Dimensional Dion-Jacobson Hybrid Organic−Inorganic Perovskite. *J. Am. Chem. Soc.* **2019**, *141* (40), 15972−15976.

(19) Mitzi, D. B. Organic−Inorganic Perovskites Containing Trivalent Metal Halide Layers: The Templating Influence of the Organic Cation Layer. *Inorg. Chem.* **2000**, *39* (26), 6107−6113.

(20) Li, M.; Li, H.; Li, W.; Li, B.; Lu, T.; Feng, X.; Guo, C.; Zhang, H.; Wei, H.; Yang, B. Oriented 2D Perovskite Wafers for Anisotropic X-Ray Detection through a Fast Tableting Strategy. *Adv. Mater.* **2022**, *34* (8), 1−9.

(21) Peng, H.; Liu, Q.; Lu, Y.-Z.; Yang, S.-J.; Qi, J.-C.; Chen, X.-G.; Liao, W.-Q. A Chiral Two-Dimensional Perovskite-like Lead-Free Bismuth(III) Iodide Hybrid with High Phase Transition Temperature. *Chem. Commun.* **2023**, *59* (68), 10295−10298.

(22) Liu, C.-D.; Fan, C.-C.; Liang, B.-D.; Zhang, W. A Polar Two-Dimensional Lead-Free Hybrid Perovskite for Self-Powered Polarization-Sensitive Photodetection. *Inorg. Chem. Front.* **2024**, *11* (15), 4611−4618.

(23) Zhang, G.; Dang, P.; Tian, L.; Yang, W.; Cheng, Z.; Lian, H.; Lin, J. Boosting Energy Transfer from Self-Trapped Exciton to Er^{3+} Through Sb^{3+} Doping in $Cs_2Na(Lu/Er)Cl_6$ Double Perovskites. *Adv. Opt. Mater.* **2023**, *11* (3), 2202369.

(24) Li, X.; Traoré, B.; Kepenekian, M.; Li, L.; Stoumpos, C. C.; Guo, P.; Even, J.; Katan, C.; Kanatzidis, M. G. Bismuth/Silver-Based Two-Dimensional Iodide Double and One-Dimensional Bi Perovskites: Interplay between Structural and Electronic Dimensions. *Chem. Mater.* **2021**, *33* (15), 6206−6216.

(25) Lehner, A. J.; Fabini, D. H.; Evans, H. A.; Hébert, C. A.; Smock, S. R.; Hu, J.; Wang, H.; Zwanziger, J. W.; Chabinyc, M. L.; Seshadri, R. Crystal and Electronic Structures of Complex Bismuth Iodides $A_3Bi_2I_9$ (A = K, Rb, Cs) Related to Perovskite: Aiding the Rational Design of Photovoltaics. *Chem. Mater.* **2015**, *27* (20), 7137−7148.

(26) Pious, J. K.; Katre, A.; Muthu, C.; Chakraborty, S.; Krishna, S.; Vijayakumar, C. Zero-Dimensional Lead-Free Hybrid Perovskite-like Material with a Quantum-Well Structure. *Chem. Mater.* **2019**, *31* (6), 1941−1945.

(27) Pious, J. K.; Muthu, C.; Dani, S.; Saeki, A.; Vijayakumar, C. Bismuth-Based Zero-Dimensional Perovskite-like Materials: Effect of Benzylammonium on Dielectric Confinement and Photoconductivity. *Chem. Mater.* **2020**, *32* (6), 2647−2652.

(28) Zhang, W.; Liu, X.; Li, L.; Sun, Z.; Han, S.; Wu, Z.; Luo, J. Triiodide-Induced Band-Edge Reconstruction of a Lead-Free Perovskite-Derivative Hybrid for Strong Light Absorption. *Chem. Mater.* **2018**, *30* (12), 4081−4088.

(29) Castro-Castro, L. M.; Guloy, A. M. Organic-Based Layered Perovskites of Mixed-Valent Gold(I)/Gold(III) Iodides. *Angew. Chem., Int. Ed.* **2003**, *42* (24), 2771−2774.

(30) Wang, H.; Qin, Z.; Xie, J.; Zhao, S.; Liu, K.; Guo, X.; Li, G.; Lu, X.; Yan, K.; Xu, J. Efficient Slantwise Aligned Dion−Jacobson Phase Perovskite Solar Cells Based on Trans-1,4-Cyclohexanediamine. *Small* **2020**, *16* (42), 2003098.

(31) Liu, Y.; Zhou, H.; Ni, Y.; Guo, J.; Lu, R.; Li, C.; Guo, X. Revealing Stability Origin of Dion-Jacobson 2D Perovskites with Different-Rigidity Organic Cations. *Joule* **2023**, *7* (5), 1016−1032.

https://doi.org/10.1021/acs.inorgchem.5c01260
Inorg. Chem. 2025, 64, 10279−10289

(32) Saraswat, A.; Vishnoi, P. 0-D and 1-D Perovskite-like Hybrid Bismuth(III) Iodides. *Chem. – Asian J.* **2024**, *19* (8), No. e202400048.
(33) Li, X.; Hoffman, J. M.; Kanatzidis, M. G. The 2D Halide Perovskite Rulebook: How the Spacer Influences Everything from the Structure to Optoelectronic Device Efficiency. *Chem. Rev.* **2021**, *121* (4), 2230−2291.
(34) Pariari, D.; Mehta, S.; Mandal, S.; Mahata, A.; Pramanik, T.; Kamilya, S.; Vidhan, A.; Guru Row, T. N.; Santra, P. K.; Sarkar, S. K.; De Angelis, F.; Mondal, A.; Sarma, D. D. Realizing the Lowest Bandgap and Exciton Binding Energy in a Two-Dimensional Lead Halide System. *J. Am. Chem. Soc.* **2023**, *145* (29), 15896−15905.
(35) Gao, L.; Li, X.; Traoré, B.; Zhang, Y.; Fang, J.; Han, Y.; Even, J.; Katan, C.; Zhao, K.; Liu, S.; Kanatzidis, M. G. *m*-Phenylenediammonium as a New Spacer for Dion−Jacobson Two-Dimensional Perovskites. *J. Am. Chem. Soc.* **2021**, *143* (31), 12063−12073.
(36) Zhang, H.-Y.; Wei, Z.; Li, P.-F.; Tang, Y.-Y.; Liao, W.-Q.; Ye, H.-Y.; Cai, H.; Xiong, R.-G. The Narrowest Band Gap Ever Observed in Molecular Ferroelectrics: Hexane-1,6-Diammonium Pentaiodobismuth(III). *Angew. Chem., Int. Ed.* **2018**, *57* (2), 526−530.
(37) Fabini, D. H.; Seshadri, R.; Kanatzidis, M. G. The Underappreciated Lone Pair in Halide Perovskites Underpins Their Unusual Properties. *MRS Bull.* **2020**, *45* (6), 467−477.
(38) Vishnoi, P.; Zuo, J. L.; Li, X.; Binwal, D. C.; Wyckoff, K. E.; Mao, L.; Kautzsch, L.; Wu, G.; Wilson, S. D.; Kanatzidis, M. G.; Seshadri, R.; Cheetham, A. K. Hybrid Layered Double Perovskite Halides of Transition Metals. *J. Am. Chem. Soc.* **2022**, *144* (15), 6661−6666.
(39) Balagowtham, N.; Acchutharaman, K. R.; Santhosh, N.; Pandian, M. S.; Ramasamy, P. Highly Stable $MAPbI_3$ Microcrystals: A Single Precursor Derived from Low-Grade PbI_2 Using Sono-Chemical Method for Economical and Efficient Perovskite Solar Cells. *J. Mater. Sci. Mater. Electron.* **2022**, *33* (27), 21531−21545.
(40) Chen, W.-J.; Chu, K.-B.; Song, J.-L. Low-Dimensional Bismuth(III) Iodide Hybrid Material with High Activity for the Fast Removal of Rhodamine B. *Acta Crystallogr. Sect. C* **2018**, *74* (12), 1744−1749.
(41) Fan, Y.; Liu, Q.; Zhang, Z.; Lien, S. Y.; Xie, Y.; Liang, W.; Gao, P. Gold-Based Double Perovskite-Related Polymorphs: Low Dimensional with an Ultranarrow Bandgap. *Chem. Mater.* **2022**, *34* (4), 1544−1553.
(42) Li, X.; Hoffman, J.; Ke, W.; Chen, M.; Tsai, H.; Nie, W.; Mohite, A. D.; Kepenekian, M.; Katan, C.; Even, J.; Wasielewski, M. R.; Stoumpos, C. C.; Kanatzidis, M. G. Two-Dimensional Halide Perovskites Incorporating Straight Chain Symmetric Diammonium Ions, $(NH_3C_mH_{2m}NH_3)(CH_3NH_3)_{n-1}Pb_nI_{3n+1}$ (m = 4−9; n = 1−4). *J. Am. Chem. Soc.* **2018**, *140* (38), 12226−12238.
(43) Zhang, W.; Liu, Z.; Zhang, L.; Wang, H.; Jiang, C.; Wu, X.; Li, C.; Yue, S.; Yang, R.; Zhang, H.; Zhang, J.; Liu, X.; Zhang, Y.; Zhou, H. Ultrastable and Efficient Slight-Interlayer-Displacement 2D Dion-Jacobson Perovskite Solar Cells. *Nat. Commun.* **2024**, *15* (1), 5709.
(44) Kumar, Y.; Sanal, K. C.; Perez, T. D.; Mathews, N. R.; Mathew, X. Band Offset Studies in $MAPbI_3$ Perovskite Solar Cells Using X-Ray Photoelectron Spectroscopy. *Opt. Mater.* **2019**, *92*, 425−431.
(45) Zhidkov, I. S.; Poteryaev, A. I.; Kukharenko, A. I.; Finkelstein, L. D.; Cholakh, S. O.; Akbulatov, A. F.; Troshin, P. A.; Chueh, C. C.; Kurmaev, E. Z. XPS Evidence of Degradation Mechanism in $CH_3NH_3PbI_3$ Hybrid Perovskite. *J. Phys.: Condens. Matter* **2020**, *32*, No. 095501.
(46) Phuyal, D.; Safdari, M.; Pazoki, M.; Liu, P.; Philippe, B.; Kvashnina, K. O.; Karis, O.; Butorin, S. M.; Rensmo, H.; Edvinsson, T.; Kloo, L.; Gardner, J. M. Electronic Structure of Two-Dimensional Lead(II) Iodide Perovskites: An Experimental and Theoretical Study. *Chem. Mater.* **2018**, *30* (15), 4959−4967.
(47) Haque, M. A.; Li, J.; Abdelhady, A. L.; Saidaminov, M. I.; Baran, D.; Bakr, O. M.; Wei, S.; Wu, T. Transition from Positive to Negative Photoconductance in Doped Hybrid Perovskite Semiconductors. *Adv. Opt. Mater.* **2019**, *7* (22), 1900865.
(48) Tailor, N. K.; Maity, P.; Satapathi, S. Observation of Negative Photoconductivity in Lead-Free $Cs_3Bi_2Br_9$ Perovskite Single Crystal. *ACS Photonics* **2021**, *8* (8), 2473−2480.
(49) Rahil, M.; Ansari, R. M.; Prakash, C.; Islam, S. S.; Dixit, A.; Ahmad, S. Ruddlesden−Popper 2D Perovskites of Type $(C_6H_9C_2H_4NH_3)_2(CH_3NH_3)_{n-1}Pb_nI_{3n+1}$ (n = 1−4) for Optoelectronic Applications. *Sci. Rep.* **2022**, *12* (1), 1−13.
(50) Wang, H.; Liu, P.; Zhang, M.; Han, B.; Wang, G.; Zhang, J.; Hu, S.; Li, H.; Guo, Y.; Zhao, G.; Gao, J.; Cheng, Z.; Wang, H. Spraying Perovskite Intermediate Enabling Inch-Scale Microwire Film Fabrication for Integration Compatible Efficient-Photodetectors Array. *Adv. Funct. Mater.* **2023**, *33* (6), 1−10.
(51) Sheldrick, G. M. Crystal Structure Refinement with SHELXL. *Acta Crystallogr. Sect. C Struct. Chem.* **2015**, *71* (1), 3−8.
(52) Song, X.; Liu, X.; Yu, D.; Huo, C.; Ji, J.; Li, X.; Zhang, S.; Zou, Y.; Zhu, G.; Wang, Y.; Wu, M.; Xie, A.; Zeng, H. Boosting Two-Dimensional $MoS_2/CsPbBr_3$ Photodetectors via Enhanced Light Absorbance and Interfacial Carrier Separation. *ACS Appl. Mater. Interfaces* **2018**, *10* (3), 2801−2809.
(53) Kresse, G.; Hafner, J. Ab Initio Molecular Dynamics for Liquid Metals. *Phys. Rev. B* **1993**, *47* (1), 558−561.
(54) Kresse, G.; Furthmüller, J. Efficient Iterative Schemes for Ab Initio Total-Energy Calculations Using a Plane-Wave Basis Set. *Phys. Rev. B* **1996**, *54* (16), 11169−11186.
(55) Kresse, G.; Joubert, D. From Ultrasoft Pseudopotentials to the Projector Augmented-Wave Method. *Phys. Rev. B* **1999**, *59* (3), 1758−1775.
(56) Monkhorst, H. J.; Pack, J. D. Special Points for Brillouin-Zone Integrations. *Phys. Rev. B* **1976**, *13* (12), 5188−5192.
(57) Sai Gautam, G.; Canepa, P.; Richards, W. D.; Malik, R.; Ceder, G. Role of Structural H_2O in Intercalation Electrodes: The Case of Mg in Nanocrystalline Xerogel-V_2O_5. *Nano Lett.* **2016**, *16* (4), 2426−2431.
(58) Sun, J.; Ruzsinszky, A.; Perdew, J. P. Strongly Constrained and Appropriately Normed Semilocal Density Functional. *Phys. Rev. Lett.* **2015**, *115* (3), 36402.
(59) Setyawan, W.; Curtarolo, S. High-Throughput Electronic Band Structure Calculations: Challenges and Tools. *Comput. Mater. Sci.* **2010**, *49* (2), 299−312.
(60) Ong, S. P.; Richards, W. D.; Jain, A.; Hautier, G.; Kocher, M.; Cholia, S.; Gunter, D.; Chevrier, V. L.; Persson, K. A.; Ceder, G. Python Materials Genomics (Pymatgen): A Robust, Open-Source Python Library for Materials Analysis. *Comput. Mater. Sci.* **2013**, *68*, 314−319.

https://doi.org/10.1021/acs.inorgchem.5c01260
Inorg. Chem. 2025, 64, 10279−10289